Journal of Solid State Chemistry 316 (2022) 123564

Contents lists available at ScienceDirect

Journal of Solid State Chemistry

journal homepage: www.elsevier.com/locate/jssc

Effect of sintering additives on the densification and dielectric properties of $Sr_{0.5}Ba_{0.5}Nb_2O_6$ ceramics synthesized by a soft-chemistry method

Roberto Köferstein *, Stefan G. Ebbinghaus

Institute of Chemistry, Martin Luther University Halle-Wittenberg, Kurt-Mothes-Straße 2, 06120, Halle, Germany

ARTICLE INFO

Keywords:
Sintering aid
Permittivity
Strontium barium niobate
Band gap
Lithium niobate
Relaxor

ABSTRACT

Nano-crystalline $Sr_{0.5}Ba_{0.5}Nb_2O_6$ powders with addition of $LiNbO_3$ or LiF as sintering additives were prepared by a soft-chemistry synthesis using polyethylene glycol. Calcination at 600 °C results in nanocrystalline powders ($d_{cryst.} \approx 30$ nm) which were sintered between 1000 and 1300 °C to ceramic bodies. By addition of 10 and 20 mol % $LiNbO_3$, the sintering temperature was reduced by about 200 K and the activation energy of the initial stage of sintering decreases from 386 to 271 kJ mol^{-1}. The sintering aid improves the grain growth and dense ceramic bodies were obtained after sintering at 1125 °C for 1 h. A higher $LiNbO_3$ content favors the formation of a pillar-like microstructure. XRD patterns of ceramics sintered above 1000 °C show only reflections of the $Sr_{0.5}Ba_{0.5}Nb_2O_6$ phase indicating an incorporation of $LiNbO_3$ in the $Sr_{0.5}Ba_{0.5}Nb_2O_6$ structure. Dielectric measurements reveal a diffuse phase transition and a relaxor-like behavior. The phase transition temperature (T_m) depends on the sintering conditions and is between 117 and 127 °C for 10 mol% $LiNbO_3$, which is very close to pure $Sr_{0.5}Ba_{0.5}Nb_2O_6$, while addition of 20 mol% shifts T_m to around 200 °C and the transition becomes slightly more diffuse. The optical band gap of the samples is ≈ 3.3 eV and depends slightly on the sintering conditions. We also tried LiF as sintering aid, but this leads to the formation of considerable amounts of secondary phases in the ceramics and relative densities of only 82%.

1. Introduction

As a lead-free and eco-friendly alternative to e.g. PZT (lead zirconate titanate), strontium barium niobate, $Sr_xBa_{1-x}Nb_2O_6$ (SBN), is an interesting candidate because of its ferroelectric, pyroelectric, piezoelectric, electro-optic, and photorefractive properties [1–4]. Due to its ferroelectric behavior, SBN is also used in magnetoelectric composites [5–7]. Furthermore, some authors report about photocatalytic activities [8,9]. $Sr_xBa_{1-x}Nb_2O_6$ is ferroelectric in the x range from 0.25 to 0.75 and crystallized in the tetragonal tungsten-bronze (TTB) structure. Its ferroelectric properties are sensitive to the composition and preparation procedure [10,11]. With rising strontium content an increasing relaxor behavior can be observed [12]. For $Sr_{0.5}Ba_{0.5}Nb_2O_6$, the permittivity maximum (T_m), which reflects the ferroelectric ⇆ paraelectric phase transition, is between 110 and 130 °C for single crystals [3,11], while for polycrystalline samples values between 40 and 177 °C have been reported [13–17].

Usually, $Sr_{0.5}Ba_{0.5}Nb_2O_6$ is synthesized by the conventional mixed-oxide method which leads to coarse-grained powders. Additionally, few soft-chemistry syntheses have been reported to produce sub-micro or nano-sized powders [14,18–21]. Compacts of strontium barium niobate reveal moderate densification behaviour. Thus, sintering to dense ceramic bodies requires high temperatures and long soaking times [14–22]. The densification behavior and the grain growth can generally be improved using sintering additives [23,24]. For example, Wang et al. [25] used SiO_2 as additive to decrease the sintering temperature. Due to the addition of SiO_2, T_m is shifted to lower temperatures. On the other hand, some authors utilized V_2O_5 as additive (liquid phase sintering) and observed an increase of T_m [26–28]. Furthermore, addition of Bi_2O_3, PbO and Nb_2O_5 enhance the densification and influence the dielectric behavior marginally [27].

In this work, we investigated the influence of $LiNbO_3$ and LiF on the sintering and dielectric behavior of $Sr_{0.5}Ba_{0.5}Nb_2O_6$. The samples were synthesized by a one-pot soft-chemistry method leading to nano-scaled preceramic powders. Phase evolution and microstructure of ceramics bodies were monitored by XRD and SEM. The sintering behavior was investigated up to 1350 °C. Additionally, the samples were characterized by diffuse reflectance and dielectric measurements.

* Corresponding author.
E-mail address: roberto.koeferstein@chemie.uni-halle.de (R. Köferstein).

https://doi.org/10.1016/j.jssc.2022.123564
Received 27 June 2022; Received in revised form 2 September 2022; Accepted 4 September 2022
Available online 9 September 2022

2. Experimental

2.1. Material preparation

All samples were synthesized according to the one-pot soft-chemistry method as described earlier [14]. The amount of the added sintering additive is related to the amount of $Sr_{0.5}Ba_{0.5}Nb_2O_6$. For the addition of $LiNbO_3$, the initial compositions of the samples were as follows: 1 mol $Sr_{0.5}Ba_{0.5}Nb_2O_6$ + x mol $LiNbO_3$ with $x = 0.1$ and 0.2 (= 3.75 and 7.50 wt%), abbreviated as SBN+LN-x.

In a typical reaction, 0.02 mol $NbCl_5$ (Alfa Aesar, 99%) was dissolved in 25 ml 2-methoxyethanol. 50 ml polyethylene glycol (PEG400) and 52 g citric acid were added under stirring on a heating plate at 150 °C until a clear solution resulted. Equimolar amounts of $SrCl_2{\cdot}6H_2O$ (Merck, ≥ 99%) and $BaCl_2{\cdot}2H_2O$ (Fluka, ≥ 99%) were solved together in 10 ml 1,2-ethanediol and $Li(CH_3COO){\cdot}2H_2O$ (Chemapol, purum) was solved in 5 ml 1,2-ethanediol. The amounts of the Sr-, Ba-, and Li-compounds are calculated as $n_{Sr} = n_{Ba} = n_{Nb}/(2[2+x])$ and $n_{Li} = n_{Nb}{\cdot}x/(2+x)$ ($x = 0.1$ and 0.2; molar fraction of $LiNbO_3$ related to the amount of $Sr_{0.5}Ba_{0.5}Nb_2O_6$). Afterwards, both the (Sr,Ba)- and Li-solutions were added to the hot Nb-solution. The reaction mixture was continuously stirred on the heating plate at 250 °C for about 3–4 h until it turned to a white highly viscous solution. The resulting (Sr,Ba,Nb,Li)-solutions were calcined at 600 °C for 2 h (rate 10 K min^{-1}) in static air leading to white nanoscaled powders. Ceramic bodies were fabricated from these powders by mixing with 10 wt% of a saturated aqueous polyvinyl alcohol (PVA) solution as pressing aid and uniaxially pressed at about 71 MPa into pellets (green density: 2.2 g cm^{-3}). These pellets were sintered on a ZrO_2 fibre mat between 1000 and 1300 °C (heating-/cooling rate 5 K min^{-1}) with a soaking time of 1 h to the final ceramic bodies. These had a thickness of about 1–1.6 mm and diameters of 4–6 mm.

For comparative purposes, pure $Sr_{0.5}Ba_{0.5}Nb_2O_6$ (abbreviated as SBN) was also prepared according to the aforementioned synthesis.

The common sintering additive LiF was also tested. For this purpose, $Sr_{0.5}Ba_{0.5}Nb_2O_6$, prepared as mentioned above, was calcined at 1100 °C for 2 h (rate 10 K min^{-1}) and mixed in a planetary mill with 76 mol% LiF (= 5.0 wt%, Sigma-Aldrich, 98%) in a polyamide jar using propane-2-ol and ZrO_2-balls. After drying, the white powder was pressed and sintered to ceramics as described above. The samples were abbreviated as SBN+LF.

2.2. Characterization

X-ray powder diffraction patterns were recorded at room temperature on a Bruker D8-Advance diffractometer, equipped with a one-dimensional silicon strip detector (LynxEye™) using Cu-K_α radiation and a counting time of 1 s per data point. Crystallite sizes and strain parameters were calculated from XRD line broadening (integral peak breadth) using the software suite WinXPOW [29] applying the Scherrer and Wilson equations. Differential thermoanalytic (DSC) investigations in flowing synthetic air (50 ml min^{-1}) were performed with a heating rate of 10 K min^{-1} using a Netzsch STA 449F5 system. Atom absorption spectroscopy measurements were carried out with an Agilent AA 280FS. Scanning electron microscope images were collected with a Phenom ProX SEM in backscattered electron mode (BSE). For impedance investigations, the ceramic bodies with a thickness of 1.2–1.4 mm were sputtered on both sides with 100 nm thick gold electrodes using a Cressington Sputter Coater 108auto. An Impedance Analyzer 4192A (Hewlett Packard) was used for frequency- and temperature dependent impedance measurements.

3. Results and discussion

LiF is used as a common sintering additive for various ceramic materials [30–34], therefore we tested LiF to reduce the sintering temperature of $Sr_{0.5}Ba_{0.5}Nb_2O_6$. Additions of 76 mol% (= 5 wt%) LiF to $Sr_{0.5}Ba_{0.5}Nb_2O_6$ leads to an enhanced densification at low sintering temperatures with relative densities of 80(1) and 82(1) % after sintering at 1050 °C and 1150 °C, whereas at 1200 °C a reduction to 77(1) % was observed. XRD investigations (Fig. S1, supporting information) of SBN+LF ceramics sintered at 1050 °C and 1200 °C leads to a mixture of $Sr_{0.5}Ba_{0.5}Nb_2O_6$, $Li_4Sr_{3.06}Nb_6O_{20}$ (JCPDS #01-089-7516), Li_2O (JCPDS #01-012-0254), and $Ba_3Nb_2O_8$ (JCPDS #01-072-0192). The fraction of secondary phases was calculated to be 25–30 wt%. For that reason, LiF is not suitable as sintering aid for $Sr_{0.5}Ba_{0.5}Nb_2O_6$.

3.1. $Sr_{0.5}Ba_{0.5}Nb_2O_6$ + $LiNbO_3$

3.1.1. Synthesis and powder characterization

In the following we used $LiNbO_3$ as sintering aid. 1 mol $Sr_{0.5}Ba_{0.5}Nb_2O_6$ + x mol $LiNbO_3$ (SBN+LN-x) with $x = 0.1$ and 0.2 were synthesized by a one-pot synthesis. To obtain white nanoscaled powders, the viscous (Sr,Ba,Nb,Li)-solutions were calcined at 600 °C for 2 h. The XRD patterns (Fig. 1) show only reflections of tetragonal $Sr_{0.5}Ba_{0.5}Nb_2O_6$ (JCPDS #01-074-6520) and rhombohedral $LiNbO_3$ (JCPDS #01-078-0250), however an increasing background level around $2\theta = 30°$ indicates an amorphous fraction in the samples. The specific surface areas (BET method) were determined to be 32(3) $m^2\ g^{-1}$ for $x = 0.1$ and 24(2) $m^2\ g^{-1}$ for $x = 0.2$, which correspond to equivalent primary particle sizes of 35(3) and 47(3) nm. The volume-weighted average crystallite size of the $Sr_{0.5}Ba_{0.5}Nb_2O_6$ phase for SBN+LN-0.1 and SBN+LN-0.2 is 31(3) and 29(3) nm, respectively.

3.1.2. Sintering, microstructure, and phase composition of the ceramics

Non-isothermal dilatometric measurements of SBN and SBN+LN-x (x = 0.1 and 0.2) powder compacts up to 1350 °C in flowing air are shown in Fig. 2. The SBN sample starts to shrink slightly at about 1100 °C while at about 1220 °C the shrinkage increases significantly. The shrinking rate achieves a maximum at 1325 °C with −1.08% min^{-1}. The SBN+LN-x compacts with the sintering additive show an improved shrinkage behavior. A first slight shrinkage begins around 700 °C, whereas a considerable densification process starts at 1150 °C (SBN+LN-0.1) and 1000 °C (SBN+LN-0.2), respectively. The shrinkage maxima are shifted to lower temperatures of 1300 °C and 1209 °C with values in both cases of −1.28% min^{-1} as shown in the inset of Fig. 2. The shrinkage rates of the three samples points to viscous flow (sliding process of whole grains) as a dominant shrinkage mechanism, because diffusion processes cause

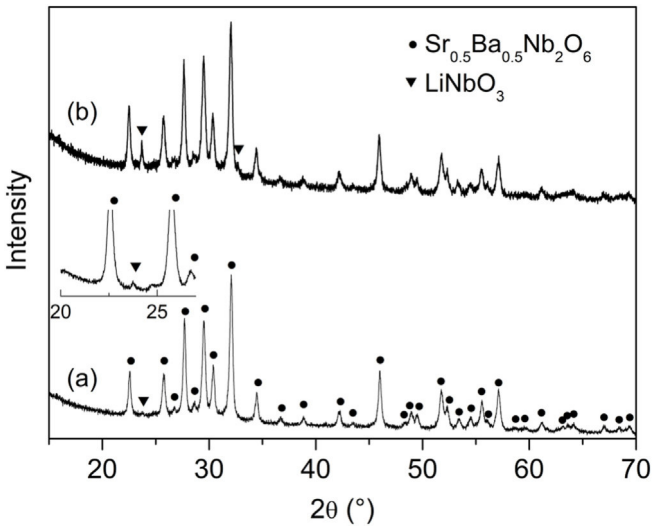

Fig. 1. Room-temperature XRD patterns of SBN+LN-x (= $Sr_{0.5}Ba_{0.5}Nb_2O_6$+x-$LiNbO_3$) powders after calcining at 600 °C for 2 h (heating rate 10 K min^{-1}): (a) $x = 0.1$, (b) $x = 0.2$. The inset shows a magnification of the XRD pattern for x = 0.1 recorded with a prolonged counting time of 10 s per data point.

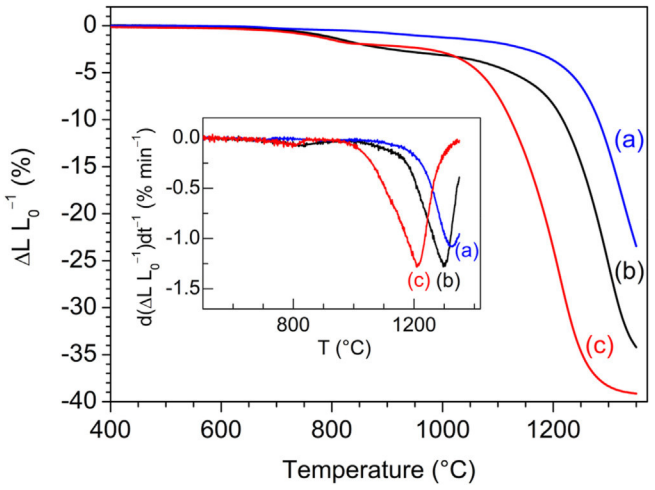

Fig. 2. Non-isothermal dilatometric measurements up to 1350 °C (heating rate 5 K min^{-1}) in flowing air of (a) SBN, (b) SBN+LN-0.1, (c) SBN+LN-0.2 of compacted powders calcined at 600 °C. The inset shows the shrinkage rates.

typical shrinkage rates between 10^{-4} and 10^{-1} % min^{-1} [35–38]. Furthermore, DSC measurements of SBN+LN-0.2 up to 1350 °C did not show any indication of the formation of a liquid phase (Fig. S2, supporting information) indicating that the densification process is caused by solid-state phase sintering. The activation energy of the initial state of sintering can be calculated from the non-isothermal dilatometric measurements applying the equation for the constant heating rate (CHR) method (1) [39,40].

$$T^2\left(\frac{d(\frac{\Delta L}{L_0})}{dt}\right) = \frac{2aE_a}{nR} \cdot \frac{\Delta L}{L_0} \quad (1)$$

where, T = temperature, $\Delta L\ L_0^{-1}$ = relative shrinkage, t = time, a = heating rate, n = constant depending on the mechanism of initial stage of sintering, E_a = activation energy, R = universal gas constant. As mentioned above, the initial stage of sintering can be described by the viscous flow mechanism ($n = 2$ [39]). Thus, E_a can be calculated from the slope by plotting the left hand-side of equation (1) versus $\Delta L\ L_0^{-1}$ (as depicted in Fig. 3). For $Sr_{0.5}Ba_{0.5}Nb_2O_6$ the activation energy for the initial stage of sintering was calculated as 386(22) kJ mol^{-1}, which is significantly lower than the activation energy of 825 kJ mol^{-1} found for coarse-grained $Sr_{0.5}Ba_{0.5}Nb_2O_6$ synthesized by the conventional mixed-oxide method [41]. By addition of $LiNbO_3$ the activation energy decreases to 300(18) and 271(15) kJ mol^{-1} for SBN+LN-0.1 and SBN+LN-0.2, respectively.

Based on these results, for further investigations the nanocrystalline powders were pressed to pellets and sintered in static air at temperatures between 1000 and 1300 °C for 1 h (heating-/cooling rate: 5 K min^{-1}). The bulk densities of the white-yellow ceramics bodies were calculated from their weight and geometric dimensions. The obtained densities are related to the single crystal density of $Sr_{0.5}Ba_{0.5}Nb_2O_6$ [42]. Dense ceramics (relative density ≥90%) of pure $Sr_{0.5}Ba_{0.5}Nb_2O_6$ can be only obtained after firing above 1300 °C. In contrast, by the addition of $LiNbO_3$ densities above 90% can be obtained already at 1175 °C ($x = 0.1$) and 1125 °C ($x = 0.2$) as shown in Fig. 4. Increasing temperatures raise the relative bulk densities further up to 96(1) %. The SBN+LN-0.2 ceramics show a very slight decrease in density after firing at 1300 °C due to a change in the microstructure as described below. In summary, the use of the sintering additive $LiNbO_3$ results in dense ceramics at significantly lower temperature and shorter sintering time, compared to pure $Sr_{0.5}Ba_{0.5}Nb_2O_6$.

Typical microstructures of SBN+LN-x ceramics are shown in Fig. 5. The average grain size ($Ø_{li}$) was estimated by counting of at least 700 grains using the lineal intercept method [43]. Ceramics with $x = 0.1$ consist of globular and irregular shaped grains. Their sizes are between 0.5 and 3.7 μm ($Ø_{li}$ = 1.7(4) μm), 1–7 μm ($Ø_{li}$ = 3.0(5) μm), and 1–18 μm ($Ø_{li}$ = 6(2) μm) after sintering at 1150, 1200, and 1300 °C, respectively. SBN+LN-0.2 samples show globular/irregular grains after sintering at 1100 °C and 1150 °C with grains sizes between 0.7 and 5.2 μm ($Ø_{li}$ = 2.3(2) μm) and 1–10 μm (Øli = 4.8(4) μm). On the other hand, sintering at 1200 °C and 1300 °C leads to a change of the microstructure. After firing at 1200 °C, we find a bimodal grain size distribution with irregular grains from 1.2 to 6 μm and few grains of about 8 μm. In addition small pillars with lengths between 1.5 and 4 μm and widths ranging from 3 to 19 μm as well as large rectangular micro crystals up to 200 μm were observed (Fig. S3, supporting information). After sintering at 1300 °C the ceramic bodies exclusively consist of pillars with dimensions similar to the ones after firing at 1200 °C and larger rectangular crystals with lengths up to 400 μm as shown in Fig. 5d.

The phase composition after sintering was examined by XRD. Fig. 6 shows the XRD patterns of SBN+LN-x sintered ceramics. After sintering at 900 °C reflections of tetragonal $Sr_{0.5}Ba_{0.5}Nb_2O_6$, and traces of orthorhombic $SrNb_2O_6$ (JCPDS #00-028-1243) are observed. Additionally, the sample with $x = 0.2$ shows the presence of rhombohedral $LiNbO_3$. The $LiNbO_3$ and $SrNb_2O_6$ reflections disappear after sintering at 1000 °C for both $x = 0.1$ and 0.2, as visible in Fig. 6c and d. Up to the highest sintering temperature of 1300 °C the XRD patterns only show reflections of the $Sr_{0.5}Ba_{0.5}Nb_2O_6$ phase (Fig. 6e,f). Even a prolonged counting time of

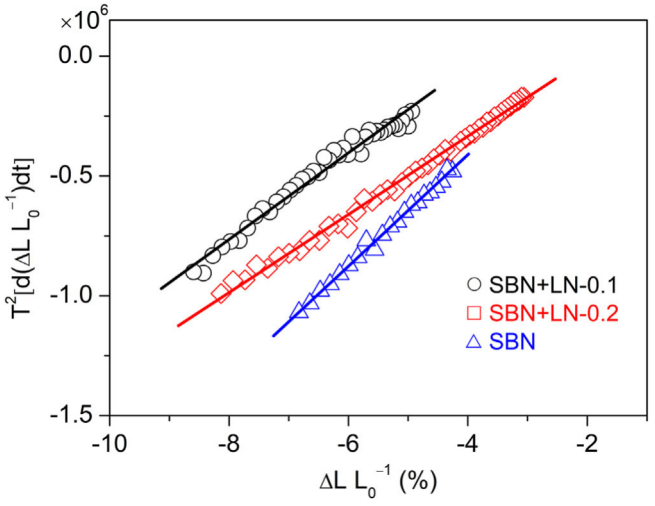

Fig. 3. Plot of $T^2[d(\Delta L\ L_0^{-1})dt$ vs. $\Delta L\ L_0^{-1}$. For the sake of clarity, every 30th data point is marked by a symbol. Solid lines are the fit results.

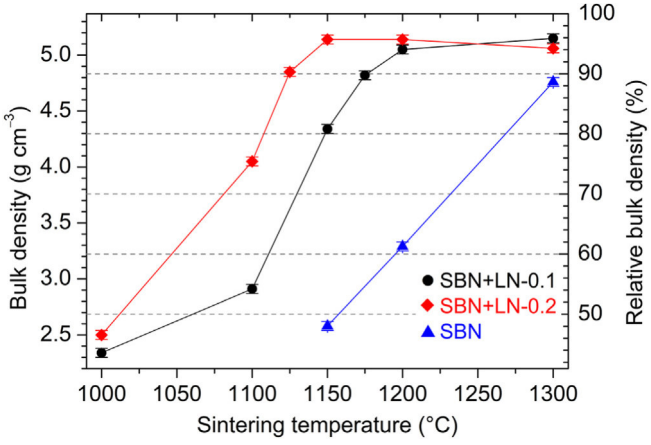

Fig. 4. Bulk densities of ceramic bodies after sintering at various temperatures for 1 h (heating-/cooling rate 5 K min^{-1}).

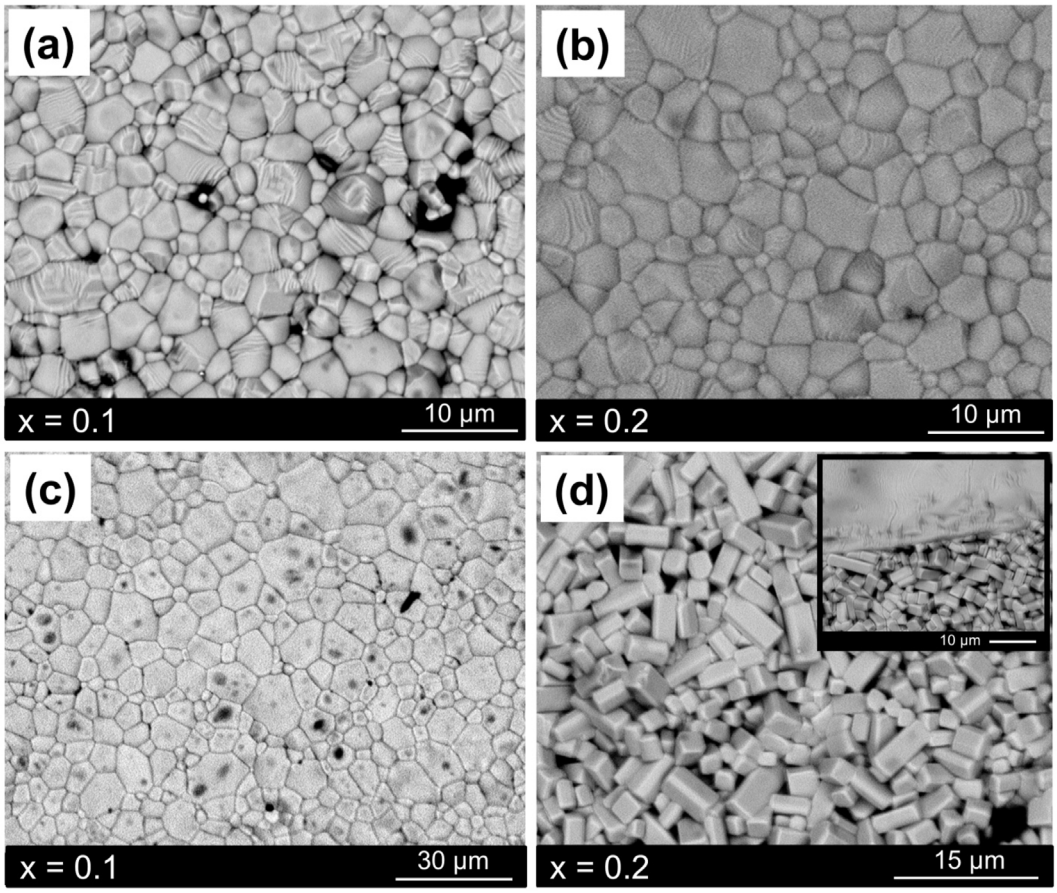

Fig. 5. SEM-BSE images of selected SBN+LN-*x* ceramic bodies sintered at different temperatures (T_s) for 1 h: (a) $T_s = 1150$ °C, (b) $T_s = 1150$ °C (c) $T_s = 1300$ °C, and (d) $T_s = 1300$ °C.

10 s per step does not reveal any traces of secondary phases (Fig. S4, supporting information) suggesting the formation of a solid solution between $Sr_{0.5}Ba_{0.5}Nb_2O_6$ and $LiNbO_3$ in the tetragonal tungsten–bronze structure which will be the subject of further investigations. The proposed formation of a solid solution is additionally supported by the absence of the melting peak of $LiNbO_3$ around 1250 °C [44,45] in the DSC measurement as mentioned above. The solid solution can be written as $Li_y(Sr_{0.5}Ba_{0.5})_{1-y/2}Nb_2O_6$, where y represents the molar fraction of $LiNbO_3$ which can be calculated from the *x* parameter as $y = x/(1+x)$. Solid solutions between SBN and (K,Na)NbO_3 has been reported by several authors [46–48]. Because of the volatility of lithium salts at high temperatures, sintering often leads to a partial sublimation of Li_2O [49–51]. For our samples, atom absorption spectroscopy indicates that the loss of lithium accounts to about 6–7% after sintering at 1300 °C for 1 h.

The optical band gap energies were obtained from diffuse reflectance spectra using the *Kubelka–Munk* theory. The optical band gap (E_g) can be described by equation (2) [52]:

$$F(R)\cdot h\nu = k(h\nu - E_g)^{1/n} \quad (2)$$

(*F(R)* – Kubelka–Munk function, *k* – energy-independent constant, E_g – optical band gap, *n* – exponent reflecting the type of transition with $n = 2$ for direct allowed transitions and $n = 0.5$ for indirect allowed transitions). As described elsewhere, $Sr_{0.5}Ba_{0.5}Nb_2O_6$ has an indirect band gap of 3.40–3.29 eV, depending on the sintering temperature [14,53]. Thus, E_g can be calculated by plotting of $(F(R) \cdot h\nu)^{0.5}$ versus $h\nu$ and extrapolating the slope to $F(R) \rightarrow 0$ (Fig. 7). Using this method, the band gap energies of SBN+LN-*x* ceramics with $x = 0.1$ were determined as 3.39(4) and 3.32(2) eV after sintering at 1100 and 1150 °C, whereas sintering at 1200 and 1300 °C gave values of 3.26(3) eV. However, in $x = 0.2$ ceramics, sintered above 1100 °C, an additional absorption feature appears at lower energies in the range between 2.4 and 3.1 eV, most likely caused by defects due the incorporation of Li^+ into the $Sr_{0.5}Ba_{0.5}Nb_2O_6$ structure [54–56]. Because of the overlapping of these two absorption regions, we used a baseline approach according to Makuła et al. [47] to derive the band gap as seen in Fig. 7. The so obtained band gaps are 3.34(2) eV after sintering at 1100 °C and 3.36(6) eV for $x = 0.2$ samples sintered between 1150 and 1300 °C. As a conclusion, the use of the sintering additive $LiNbO_3$ does not lead to a considerable change of the band gap compared to pure $Sr_{0.5}Ba_{0.5}Nb_2O_6$ [14].

3.1.3. Impedance spectroscopy

Fig. 8 shows the evolution of the relative permittivity (ε_r') and dissipation factor (tan δ) with temperature for ceramic bodies with $x = 0.1$ at 1 kHz. Samples fired at 1150, 1200, and 1300 °C show diffuse ferroelectric ⇆ paraelectric phase transitions with broad maxima at 127(1), 117(1), and 118(1) °C, close to pure $Sr_{0.5}Ba_{0.5}Nb_2O_6$ [3,14]. The ε_r' values at these maxima increases with sintering temperature from 1362(123) to 3135(282) most likely caused by increasing grain sizes and densities. Fig. 9 shows the temperature (T_m) of the permittivity maxima depending on frequencies. T_m is shifted towards higher temperatures with increasing frequencies due to the relaxor-like behavior of the samples [57,58]. The shift of T_m in the range from 1 kHz to 3 MHz is 6(2) K for the sample sintered at 1150 °C and increases to 11(2) K after sintering at 1300 °C (inset in Fig. 9).

The evolution of the permittivity depending on temperature for SBN+LN-0.2 ceramics can be seen in Fig. 10a. The samples with $x = 0.2$ show a shift of T_m towards higher temperatures. Sintering at 1100 °C does not lead to a clear phase transition at 1 kHz, whereas frequencies

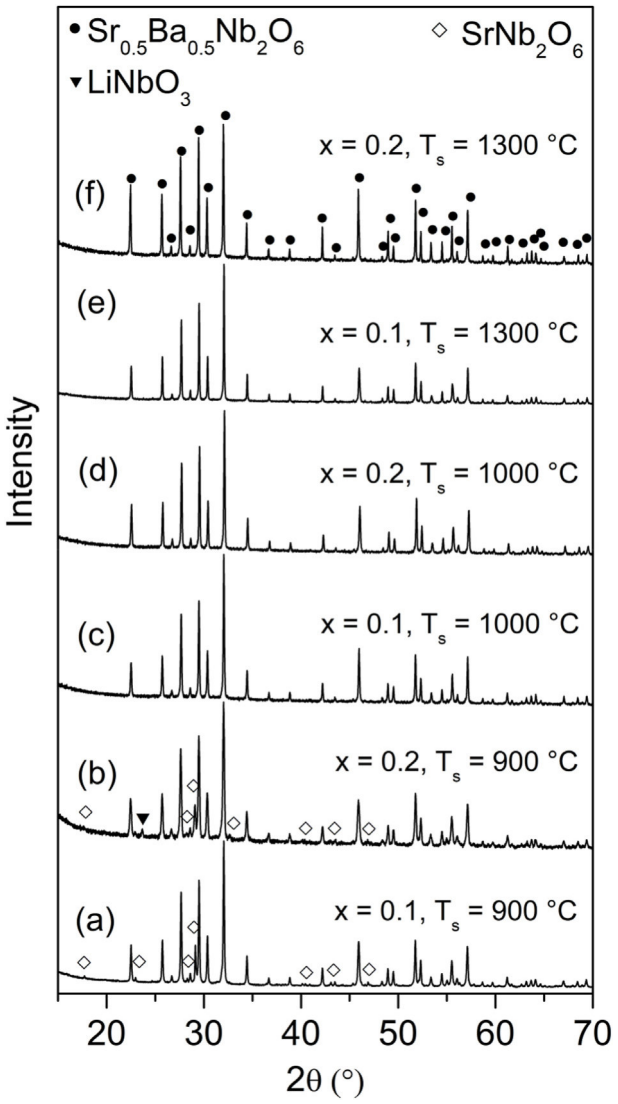

Fig. 6. Room-temperature XRD patterns of SBN+LN-*x* ceramics after sintering at different temperatures (T_s) for 1 h (heating-/cooling rate 5 K min^{-1}).

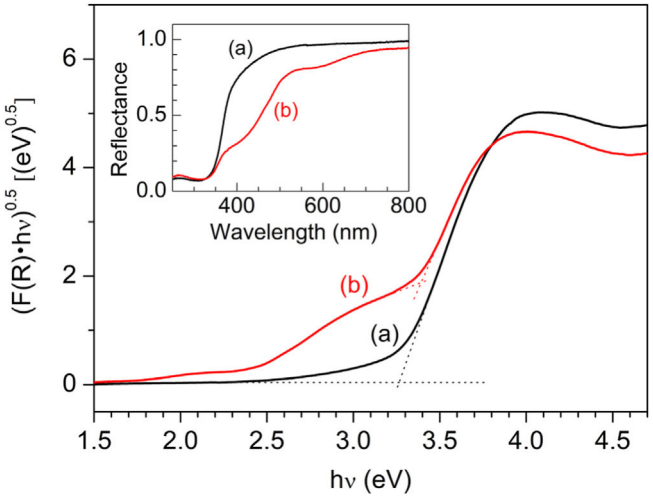

Fig. 7. $(F(R) \cdot h\nu)^{0.5}$ versus $h\nu$ of SBN+LN-*x* ceramics sintered at 1200 °C for 1 h. (a) $x = 0.1$, (b) $x = 0.2$. The inset shows the diffuse reflectance spectra.

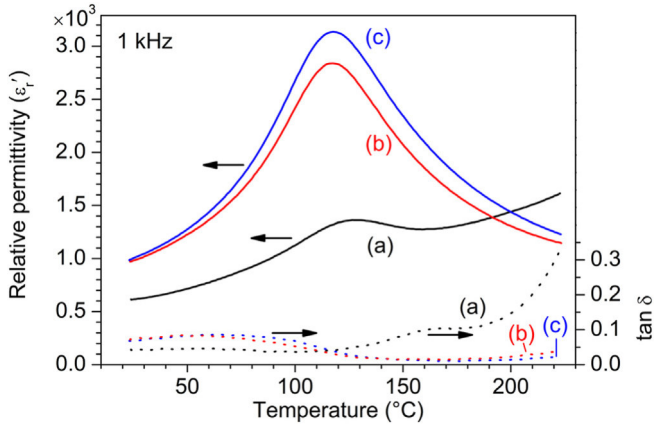

Fig. 8. Temperature dependence of the real part of the relative permittivity (ε_r') and tan δ at 1 kHz of SBN+LN-0.1 ceramic bodies sintered for 1 h at: (a) 1150 °C, (b) 1200 °C, and (c) 1300 °C. The uncertainty of the data is smaller than the symbol size and is lower than 5%.

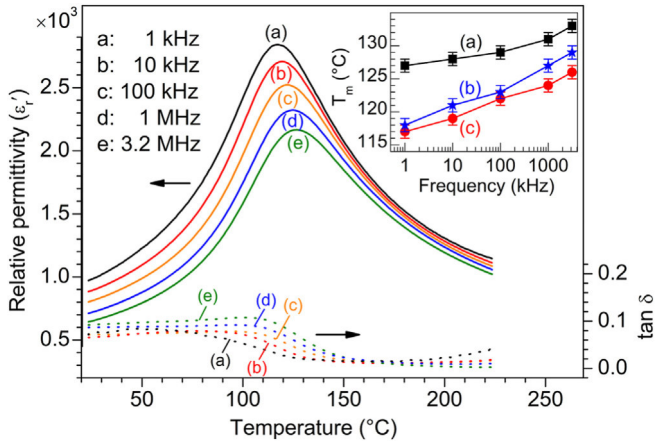

Fig. 9. Temperature dependence of the relative permittivity (ε_r') and the dissipation factor (tan δ) at various frequencies for SBN+LN-0.1 sintered at 1200 °C for 1 h. The inset shows the temperature of the permittivity maximum (T_m) depending on frequency and sintering temperature for samples sintered at: (a) 1150 °C, (b) 1200 °C, and (c) 1300 °C. The uncertainty of the data is smaller than the symbol size and is lower than 5%.

above 1 kHz reveal a maximum at 213(2) °C (Fig. 10b and Fig. S5, supporting information). The permittivity maximum of the dense ceramic, sintered at 1150 °C ($x = 0.2$), appears at 196(2) °C with $\varepsilon_r' = 3071(277)$ at 1 kHz and shifts to 200(2) °C at 3 MHz with $\varepsilon_r' = 2580(232)$ (Fig. S6, supporting information). The development of ε_r' for samples ($x = 0.2$) sintered at 1200 and 1300 °C shows only at frequencies ≥100 kHz a clear permittivity maximum at 223(2) and 221(2) °C corresponding to the diffuse ferroelectric ⇆ paraelectric phase transition (Figs. S7 and S8, supporting information). Moreover, both the considerable shift of T_m to higher temperatures and the reduction of the permittivity maxima after sintering from 1150 to 1300 °C correlates with the appearance of a pillar-like microstructure as also observed in pure $Sr_{0.5}Ba_{0.5}Nb_2O_6$ [14]. Frequency-dependent dielectric measurements at room temperature (23 °C) in the range from 0.5 kHz to 10 MHz are shown in Fig. 11. The samples show decreasing permittivity values with rising frequency, while the dissipation factor (tan δ) slightly increases. The ε_r' values of the $x = 0.1$ ceramics (Fig. 11a) rise with sintering temperature caused by an increase in density and grain sizes. However, a different behavior can be observed for $x = 0.2$ ceramics (Fig. 11b). Sintering from 1100 to 1150 °C results in larger permittivities, while firing at 1200 and 1300 °C leads to significant lower ε_r' values, due to the change in microstructure after

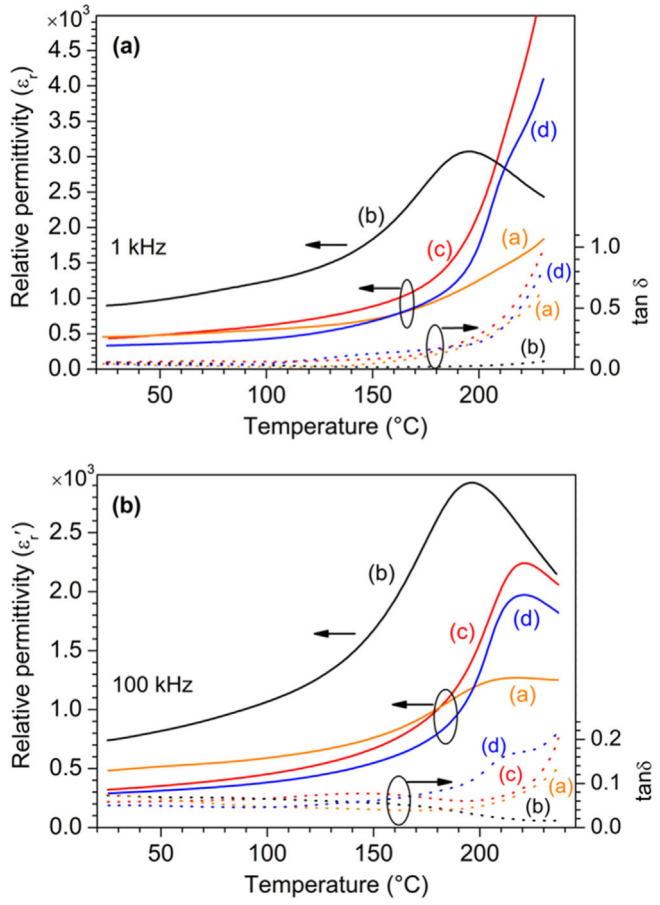

Fig. 10. Temperature dependence of the real part of ε_r' and tan δ at 1 kHz **(a)** and 100 kHz **(b)** of SBN+LN-0.2 ceramic bodies sintered for 1 h at: (a) 1100 °C, (b) 1150 °C, (c) 1200 °C and (d) 1300 °C. The uncertainty of the data is smaller than the symbol size and is lower than 5%.

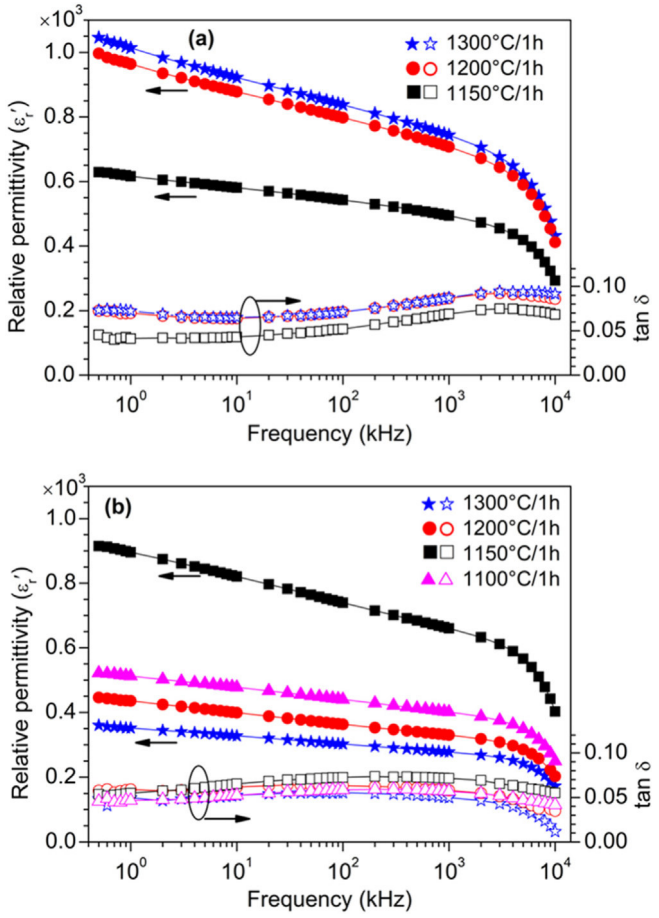

Fig. 11. Frequency dependence of the real part of ε_r' and the dissipation factor at 23 °C for SBN+LN-x ceramic bodies sintered at the indicated temperatures. **(a)** $x = 0.1$, **(b)** $x = 0.2$. The uncertainty of the data is smaller than the symbol size and is lower than 5%.

sintering at these temperatures as mentioned above. The ceramics sintered at 1200 °C ($x = 0.2$) consist of globular/irregular grains along with pillar-like grains which effects higher ε_r' values compared to those sintered at 1300 °C, which only show pillar-like grains. Decreasing permittivity values by changing from a globular/irregular to a pillar-like microstructure were also observed in $Sr_{0.5}Ba_{0.5}Nb_2O_6$ ceramics [14].

The dielectric behavior of a relaxor ferroelectric can be expressed by the following Curie-Weiss type law (3) [59]:

$$\frac{1}{\varepsilon} - \frac{1}{\varepsilon_m} = \frac{(T - T_m)^\gamma}{C'} \tag{3}$$

where, ε_m is the permittivity maximum, T_m is the temperature at ε_m, C′ is a constant, and the exponent γ is the diffuseness coefficient. Thus, γ can be obtained from a plot of $\ln(\varepsilon^{-1} - \varepsilon_m^{-1})$ versus $\ln(T - T_m)$. $x = 0.1$ ceramics reveal diffuseness coefficients between 1.7 and 1.8, which is comparable with pure $Sr_{0.5}Ba_{0.5}Nb_2O_6$ [14], whereas $x = 0.2$ samples show a slightly larger γ value of 1.8–1.9. Larger γ values indicate an increasing degree of lattice disorder most likely due to formation of a solid solution between $LiNbO_3$ and $Sr_{0.5}Ba_{0.5}Nb_2O_6$ [60,61].

The discussion above is based on the model of a lossy capacitor and does not consider a possible dc-conductivity. At elevated temperatures the ceramics show considerable dc-conductivities suggesting a semiconducting nature. As reported elsewhere [62] for a single resistance-capacitor (RC) element, the specific impedance (ρ^*) is described by equation (4):

$$\rho^* = \frac{\rho_{dc}}{1 + (i\omega\tau)^\beta} \tag{4}$$

(β – constant phase shift (CPE) coefficient, $\tau = \rho_{dc}\varepsilon\varepsilon_0$). The high-temperature impedance data were modelled using equivalent circuits consisting of one or two parallel resistance-capacitor (RC) elements. For $x = 0.2$ ceramics sintered at 1200 and 1300 °C, the impedance data reveal two semicircle arcs, which can be described by two parallel connected RC-elements suggesting two different relaxation processes (Fig. 12). The two obtained relative permittivities for each of these ceramics are $13{\cdot}10^3$ and $27{\cdot}10^4$ sintered at 1200 °C, whereas values of and $9{\cdot}10^3$ and $17{\cdot}10^4$ were found after sintering at 1300 °C. The smaller values can be related to bulk contributions, while the larger values most likely corresponds to grain boundary effects, as, according to Irvine et al. [63], the bulk permittivity is at least one order of magnitude lower than grain boundary permittivity. Cole-Cole plots for the other ceramic samples (Fig. S9 and Fig. S10, supporting information) show single semicircle arcs indicating a single relaxation process. Because of the calculated permittivities between $1.6{\cdot}10^3$ and $3.5{\cdot}10^3$ these values can be assigned to the bulk effect, showing that grain boundary contributions play a negligible role in these samples.

Due to the addition of $LiNbO_3$, we observed an increase of the permittivity maximum up to 50% and a considerable shift of T_m for $x = 0.2$, compared to pure $Sr_{0.5}Ba_{0.5}Nb_2O_6$ [14].

4. Conclusion

$Sr_{0.5}Ba_{0.5}Nb_2O_6$ ceramics with the addition of 10 and 20 mol%

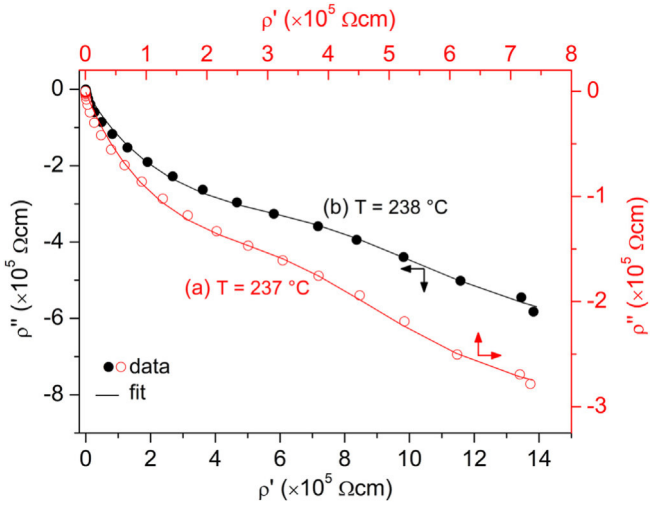

Fig. 12. Cole-Cole plots measured at the indicated temperatures of SBN+LN-0.2 ceramic bodies sintered for 1 h at (a) 1200 °C and (b) 1300 °C. Fits were carried out using two parallel connected RC-elements. Lines are the respective fit results, while symbols correspond to experimental data. The uncertainty of the data is smaller than the symbol size and is lower than 5%.

$LiNbO_3$ as sintering aid were synthesized by a one-pot method using PEG400. Calcining at 600 °C results in white nanocrystalline powders with crystallite sizes of 31(3) and 29(3) nm and specific surface areas of 32(3) and 24(2) $m^2\ g^{-1}$. Dilatometric measurements on powder compacts show that the sintering starts at significant lower temperatures with addition of $LiNbO_3$. The activation energies for the initial stage of sintering were calculated as 300(18) and 271(15) kJ mol^{-1} for 10 and 20 mol% $LiNbO_3$, respectively, while $Sr_{0.5}Ba_{0.5}Nb_2O_6$ without any sintering additive reveals an activation energy of 386(22) kJ mol^{-1}. Dense ceramic bodies were obtained after sintering at 1125 °C, which is about 200 K lower than for $Sr_{0.5}Ba_{0.5}Nb_2O_6$ ceramics without any sintering aid. XRD and DSC measurements indicate the incorporation of $LiNbO_3$ into the $Sr_{0.5}Ba_{0.5}Nb_2O_6$ structure by forming a solid solution during sintering. Temperature and frequency-dependent dielectric investigations show a diffuse ferroelectric ⇆ paraelectric phase transition and a relaxor behavior. The dielectric maximum (T_m) slightly depends on the sintering temperature. T_m is around 120–130 °C for the addition of 10 mol% $LiNbO_3$ and shifts to about 200 °C for 20 mol%.

$LiNbO_3$ as sintering additive considerably reduced the sintering temperatures of $Sr_xBa_{1-x}Nb_2O_6$ ceramics without the formation of a liquid phase. Due to the additive, the phase transition temperature (T_m) and the grain sizes can be easily tuned. $LiNbO_3$ is also a potential candidate as sintering aid in $Sr_xBa_{1-x}Nb_2O_6$ based magnetoelectric composites.

CRediT authorship contribution statement

Roberto Köferstein: Conceptualization, Data curation, Formal analysis, Investigation, Project administration, Resources, Validation, Visualization, Writing – original draft, Writing – review & editing. **Stefan G. Ebbinghaus:** Conceptualization, Project administration, Resources, Supervision, Validation, Writing – original draft.

Declaration of competing interest

The authors declare that they have no known competing financial interests or personal relationships that could have appeared to influence the work reported in this paper.

Data availability

Data will be made available on request.

Acknowledgments

We are grateful to Dr. F. Oehler for AAS investigations.

Appendix A. Supplementary data

Supplementary data to this article can be found online at https://doi.org/10.1016/j.jssc.2022.123564.

References

[1] A.M. Glass, Investigation of the electrical properties of $Sr_{1-x}Ba_xNb_2O_6$ with special reference to pyroelectric detection, J. Appl. Phys. 40 (1969) 4699–4713.
[2] D. Rytz, B.A. Wechsler, R.N. Schwartz, C.C. Nelson, C.D. Brandle, A.J. Valentino, G.W. Berkstresser, Temperature dependence of photorefractive properties of strontium-barium niobate ($Sr_{0.6}Ba_{0.4}Nb_2O_6$), J. Appl. Phys. 66 (1989) 1920–1924.
[3] T. Lukasiewicz, M.A. Swirkowicz, J. Dec, W. Hofman, W. Szyrski, Strontium–barium niobate single crystals, growth and ferroelectric properties, J. Cryst. Growth 310 (2008) 1464–1469.
[4] R.R. Neurgaonkar, L.E. Cross, Piezoelectric tungsten bronze crystals for SAW device applications, Mater. Res. Bull. 21 (1989) 893–899.
[5] S. Tiwari, S. Vitta, Magnetoelectric and magnetodielectric coupling and microwave resonator characteristics of $Ba_{0.5}Sr_{0.5}Nb_2O_6/CoCr_{0.4}Fe_{1.6}O_4$ multiferroic composite, Sci. Rep. 8 (2018), 11619.
[6] X.M. Chen, Y.H. Tang, I.-W. Chen, Z.C. Xu, S.Y. Wu, Dielectric and magnetoelectric characterization of $CoFe_2O_4/Sr_{0.5}Ba_{0.5}Nb_2O_6$ composites, J. Appl. Phys. 96 (2004) 6520–6522.
[7] R. Köferstein, F. Oehler, S.G. Ebbinghaus, Fine-grained magnetoelectric $Sr_{0.5}Ba_{0.5}Nb_2O_6-CoFe_2O_4$ composites synthesized by a straightforward one-pot method, Mater. Chem. Phys. 278 (2022), 125616.
[8] G. Han, S. Cao, B. Lin, UV photocatalytic activity for water decomposition of $Sr_xBa_{1-x}Nb_2O_6$ nanocrystals with different components and morphologies, J. Chem. (2017), 2163608.
[9] K. Yoshida, H. Masai, Y. Takahashi, R. Ihara, T. Fujiwara, Fabrication of $Sr_{0.5}Ba_{0.5}Nb_2O_6$-precipitated microstructured ceramics for photocatalytic application, J. Ceram. Soc. Jpn. 119 (2011) 731–735.
[10] S.-I. Kang, J.-H. Lee, J.-J. Kim, H.Y. Lee, S.-H. Cho, Effect of sintering atmosphere on densification and dielectric characteristics in $Sr_{0.5}Ba_{0.5}Nb_2O_6$ ceramics, J. Eur. Ceram. Soc. 24 (2004) 1031–1035.
[11] A.A. Ballmann, H. Brown, The growth and properties of strontium barium metaniobate $Sr_xBa_{1-x}Nb_2O_6$, A tungsten bronze ferroelectric, J. Cryst. Growth 1 (1967) 311–314.
[12] W.H. Huang, Dwight Viehland, R.R. Neurgaonkar, Anisotropic glasslike characteristics of strontium barium niobate relaxors, J. Appl. Phys. 76 (1994) 490–496.
[13] S.H. Kshirsagar, A.N. Tarale, S.R. Jigajeni, D.J. Salunkhe, P.B. Joshi, Effect of Ni doping on ferroelectric, dielectric and magneto dielectric properties of strontium barium niobate ceramics, Indian J. Pure Appl. Phys. 53 (2015) 119–124.
[14] R. Köferstein, F. Oehler, S.G. Ebbinghaus, Investigations of nano-crystalline $Sr_{0.5}Ba_{0.5}Nb_2O_6$ and bulk ceramics synthesized by a polymerization method using PEG400, J. Eur. Ceram. Soc. 39 (2019) 1156–1163.
[15] M. Said, T.S. Velayutham, W.C. Gan, W.H. Abd Majid, The structural and electrical properties of $Sr_xBa_{(1-x)}Nb_2O_6$ (SBN) ceramic with varied composition, Ceram. Int. 41 (2015) 7119–7124.
[16] P.K. Patro, A.R. Kulkarni, C.S. Harendranath, Microstructure and dielectric properties of strontium barium niobate ceramics synthesized by partial coprecipitation, J. Eur. Ceram. Soc. 23 (2003) 1329–1335.
[17] T. Chen, S.Y. Wu, X.Q. Liu, X.M. Chen, A novel sol–gel route to synthesize $(Sr_{0.5}Ba_{0.5})Nb_2O_6$ ceramics with enhanced electrocaloric effect, J. Adv. Dielectr. 7 (2017), 1750012.
[18] A.B. Panda, A. Pathak, P. Pramanik, Low temperature preparation of nanocrystalline solid solution of strontium–barium–niobate by chemical process, Mater. Lett. 52 (2002) 180–186.
[19] S.R. Dhage, R. Pasricha, V. Ravi, Synthesis of $Sr_{0.5}Ba_{0.5}Nb_2O_6$ by urea method, Mater. Lett. 59 (2005) 1053–1055.
[20] R. Pasricha, V. Ravi, Synthesis of $Sr_{0.5}Ba_{0.5}Nb_2O_6$ by citrate gel method, mater, Chem. Phys. 94 (2005) 34–36.
[21] C.M. Dudhe, S.B. Nagdeot, C.P. Chaudhari, Ferroelectric domains in $Sr_{0.5}Ba_{0.5}Nb_2O_6$ (SBN50) at nanolevel, Ferroelectrics 482 (2015) 104–112.
[22] S.B. Deshpande, H.S. Potdar, P.D. Godbole, S.K. Date, Preparation and ferroelectric properties of SBN:50 ceramics, J. Am. Ceram. Soc. 75 (1992) 2581–2585.
[23] R. Köferstein, L. Jäger, M. Zenkner, H.-P. Abicht, Preparation and sintering behaviour of a fine grain $BaTiO_3$ powder containing 10 mol% $BaGeO_3$, J. Mater. Sci. 43 (2008) 832–838.
[24] A. Talimian, H.F. El-Maghraby, M. Michálkova, D. Galusek, Sintering and grain growth behaviour of magnesium aluminate spinel: effect of lithium hydroxide addition, J. Eur. Ceram. Soc. 41 (2021) 5634–5643.

[25] L. Wang, S. Wanmei, M. Kunchang, L. Shijun, Effect of silica sintering additive on the sintering behavior and dielectric properties of strontium barium niobate ceramics, J. Eur. Ceram. Soc. 29 (2009) 1427–1432.
[26] Q.W. Huang, L.H. Zhu, J. Xu, P.L. Wang, H. Gu, Y.B. Cheng, Effect of V_2O_5 on sintering behaviour, microstructure and dielectric properties of textured $Sr_{0.4}Ba_{0.6}Nb_2O_6$ ceramics, J. Eur. Ceram. Soc. 25 (2005) 957–962.
[27] S. Nishiwaki, J. Takahashi, K. Kodaira, Effect of additives on microstructure development and ferroelectric properties of $Sr_{0.3}Ba_{0.7}Nb_2O_6$ ceramics, Jpn. J. Appl. Phys. 33 (1994) 5477–5481.
[28] A.Y. Oral, M.L. Mecartney, Properties of sol-gel derived strontium barium niobate ceramics and the effect of V_2O_5 additive, J. Mater. Sci. 36 (2001) 5519–5527.
[29] Program WinXPOW v2.11, Stoe & Cie GmbH, Darmstadt, 2004.
[30] U. Intatha, S. Eitssayeam, K. Pengpat, K.J.D. MacKenzie, T. Tunkasiri, Dielectric properties of low temperature sintered LiF doped $BaFe_{0.5}Nb_{0.5}O_3$, Mater. Lett. 61 (2007) 196–200.
[31] S. Balabanov, D. Permin, T. Evstropov, P. Andreev, L. Basyrova, P. Camy, M. Baranov, X. Mateos, P. Loiko, Hot pressing of Yb:Y_2O_3 laser ceramics with LiF sintering aid, Opt. Mater. 119 (2021), 111349.
[32] Y. Lai, H. Su, G. Wang, X. Tang, X. Huang, X. Liang, H. Zhang, Y. Li, K. Huang, X.R. Wang, Low-temperature sintering of microwave ceramics with high *Qf* values through LiF addition, J. Am. Ceram. Soc. 102 (2019) 1983, 1903.
[33] J.P. Guha, H.U. Anderson, Reaction during sintering of barium titanate with lithium fluoride, J. Am. Ceram. Soc. 69 (1986) C193–C194.
[34] J.M. Huassonne, G. Desgardin, Ph Bajolet, B. Raveau, Barium titanate perovskite sintered with lithium fluoride, J. Am. Ceran. Soc. 66 (1983) 801–807.
[35] R. Köferstein, L. Jäger, M. Zenkner, T. Müller, H.-P. Abicht, Shrinkage mechanism and phase evolution of fine-grain $BaTiO_3$ powder compacts containing 10 mol% $BaGeO_3$ prepared via a precursor route, Mater. Chem. Phys. 112 (2008) 531–535.
[36] W. Schatt, Sintervorgänge, VDI-Verlag, Düsseldorf, 1992, pp. 78–100.
[37] W. Schatt, E. Friedrich, Dislocation activated sintering processes, Powder Metall. 28 (1985) 140–144.
[38] W. Schatt, B. Vetter, E. Friedrich, Non-isothermal shrinkage of compacts, Powder Metall. 34 (1991) 179–182.
[39] L.A. Pérez-Maqueda, J.M. Criado, C. Real, Kinetics of the initial stage of sintering from shrinkage data: simultaneous determination of activation energy and kinetic model from a single nonisothermal experiment, J. Am. Ceram. Soc. 85 (2002) 763–768.
[40] J.L. Woolfrey, M.J. Bannister, Nonisothermal techniques for studying initial-stage sintering, J. Am. Soc. 55 (1972) 390–394.
[41] J.-T. Sgiue, T.-T. Fang, The sintering behavior of CeO_2-doped strontium barium niobate ceramics, J. Eur. Ceram. Soc. 22 (2002) 1705–1709.
[42] G.W. Marks, L.A. Monson, Effect of certain group IV oxides on dielectric constant and dissipation factor of barium titanate, Ind. Eng. Chem. 47 (1955) 1611–1620.
[43] M.I. Mendelson, J. Am. Ceram. Soc. 52 (1969) 443–446.
[44] R.L. Byer, J.F. Young, R.S. Feigelson, Growth of high-Quality $LiNbO_3$ crystals from the congruent melt, J. Appl. Phys. 41 (1970) 2320–2325.
[45] B.A. Scott, G. Burns, Determination of stoichiometry variations in $LiNbO_3$, and $LiTaO_3$, by Raman powder spectroscopy, J. Am. Ceram. Soc. 55 (1972) 225–230.
[46] Y.B. Yao, C.L. Mak, B. Ploss, Phase transitions and electrical characterizations of $(K_{0.5}Na_{0.5})_{2x}(Sr_{0.6}Ba_{0.4})_{5-x}Nb_{10}O_{30}$ (KNSBN) ceramics with 'unfilled' and 'filled' tetragonal tungsten–bronze (TTB) crystal structure, J. Eur. Ceram. Soc. 320 (2012) 4353–4361.
[47] Y. Jiang, R. Guo, A.S. Bhalla, Single crystal growth and ferroelectric properties of $\alpha(Ba_{1-x}Sr_x)Nb_2O_6$:$\beta(Na_{1-y}K_y)NbO_3$ solid solutions, J. Appl. Phys. 84 (1998) 5140–5146.
[48] R.R. Neurgaonkar, W.K. Cory, J.R. Oliver, W.W. Clark III, G.L. Wood, M.J. Miller, E.J. Sharp, Growth and ferroelectric properties of tungsten bronze $Ba_{2-x}Sr_xK_{1-y}Na_yNb_5O_{15}$ (BSKNN) single crystals, J. Cryst. Growth 84 (1987) 629–637.
[49] A.Z. Simões, A.H.M. González, A.A. Cavalheiro, M.A. Zaghete, B.D. Stojanovic, J.A. Varela, Effect of magnesium on structure and properties of $LiNbO_3$ prepared from polymeric precursors, Ceram. Int. 28 (2002) 265–270.
[50] R. Köferstein, Thermoanalytical, optical, and magnetic investigations on nanocrystalline $Li_{0.5}Fe_{2.5}O_4$ and resulting ceramics prepared by a starch-based soft-chemistry synthesis, J. Solid State Chem. 287 (2020), 121380.
[51] E. Antolini, Lithium loss from lithium cobalt oxide: hexagonal $Li_{0.5}Co_{0.5}O$ to cubic $Li_{0.065}Co_{0.935}O$ phase transition, Int. J. Inorg. Mater. 3 (2001) 721–726.
[52] R. Köferstein, T. Buttlar, S.G. Ebbinghaus, Investigationson $Bi_{25}FeO_{40}$ powders synthesized by hydrothermal and combustion-like processes, J. Solid State Chem. 217 (2014) 50–56.
[53] J. Hormadaly, S.N. Subbarao, R. Kershaw, K. Dwight, A. Wold, Preparation and comparison of the photoelectronic properties of $Sr_2Nb_2O_7$ and $Ba_{0.5}Sr_{0.5}Nb_2O_6$, J. Solid State Chem. 33 (1980) 27–32.
[54] V. Sa-Yakanit, H.R. Glyde, Urbach tails and disorder, comments cond, Mat. Phys. 13 (1987) 35–48.
[55] P. Makuła, M. Pacia, W. Macyk, How to correctly determine the band gap energy of modified semiconductor photocatalysts based on UV−Vis spectra, J. Phys. Chem. Lett. 9 (2018) 6814–6817.
[56] F.P. Koffyberg, K. Dwight, A. Wold, Interband transition of semiconducting oxides determined from photoelectrolysis spectra, Solid State Commun. 30 (1979) 433–437.
[57] L.E. Cross, Relaxor ferroelectrics: an overview, Ferroelectrics 151 (1994) 305–320.
[58] T. Tsurumi, K. Soejima, T. Kamiya, M. Daimon, Mechanism of diffuse phase transition in relaxor ferroelectrics, Jpn. J. Appl. Phys. 33 (1994) 1959–1964.
[59] K. Uchino, S. Nomura, Critical exponents of the dielectric constants in diffused phase-transition crystals, Ferroelectrics 44 (1982) 55–61.
[60] X. Qin, D. Shihu, S. Tianxiu, W. Homgni, Diffuse phase transition of $Ba_{0.92}Ca_{0.08}(Ti_{0.82}Zr_{0.18})O_3$ based ceramics, Ferroelectrics 426 (2012) 282–289.
[61] L.E. Cross, Relaxor Ferroelectrics, Ferroelectrics 76 (1987) 242–267.
[62] F. Oehler, H.-T. Langhammer, S.G. Ebbinghaus, Preparation and dielectric properties of $CaTaO_2N$ and $SrNbO_2N$ ceramics, J. Eur. Ceram. Soc. 37 (2017) 2129–2136.
[63] J.T.S. Irvine, D.C. Sinclair, A.R. West, Electroceramics: characterization by impedance spectroscopy, Adv. Mater. 2 (1990) 132–138.

Supporting Information

Effect of sintering additives on the densification and dielectric properties of $Sr_{0.5}Ba_{0.5}Nb_2O_6$ ceramics synthesized by a soft-chemistry method

Roberto Köferstein* and Stefan G. Ebbinghaus

Institute of Chemistry, Martin Luther University Halle-Wittenberg,

Kurt-Mothes-Straße 2, 06120 Halle, Germany.

* Corresponding author

Tel.: +49-345-5525630; Fax: +49-345-5527028.

E-mail address: roberto.koeferstein@chemie.uni-halle.de

The following abbreviations were used:
SBN+LF – $Sr_{0.5}Ba_{0.5}Nb_2O_6$ + 0.76 LiF
SBN+LiN-0.1 – $Sr_{0.5}Ba_{0.5}Nb_2O_6$ + 0.1 $LiNbO_3$
SBN+LiN-0.2 – $Sr_{0.5}Ba_{0.5}Nb_2O_6$ + 0.2 $LiNbO_3$

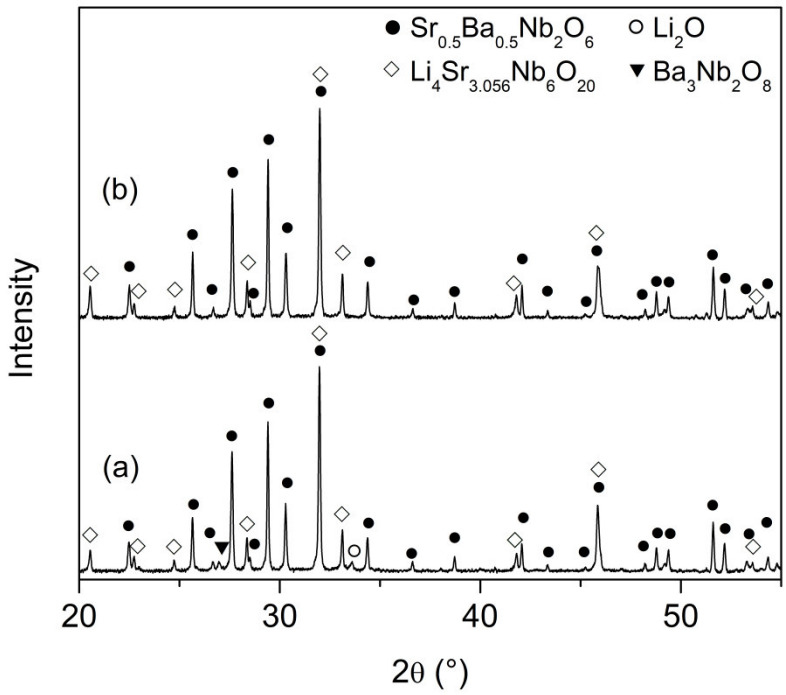

Fig. S1: Room-temperature XRD patterns of SBN-LF ceramics after sintering for 1 h at (a) 1050 °C, (b) 1200 °C.

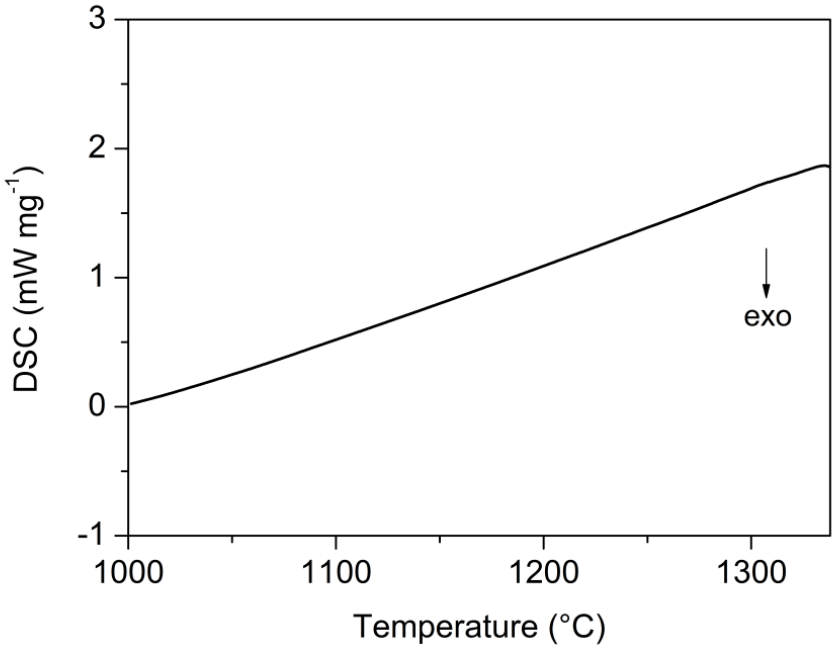

Fig. S2: DSC measurement of SBN+LN-0.2 compact in flowing air.

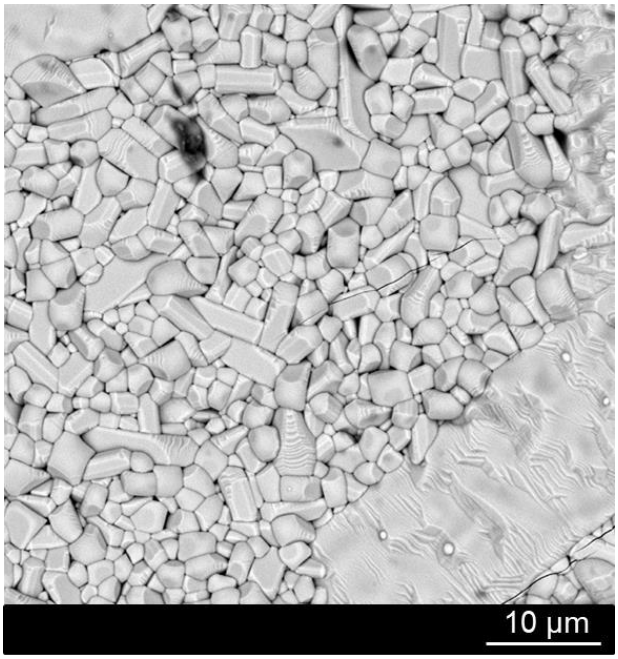

Fig. S3: SEM-BSE image of a SBN+LiN-0.2 ceramic body sintered at 1200 °C for 1 h.

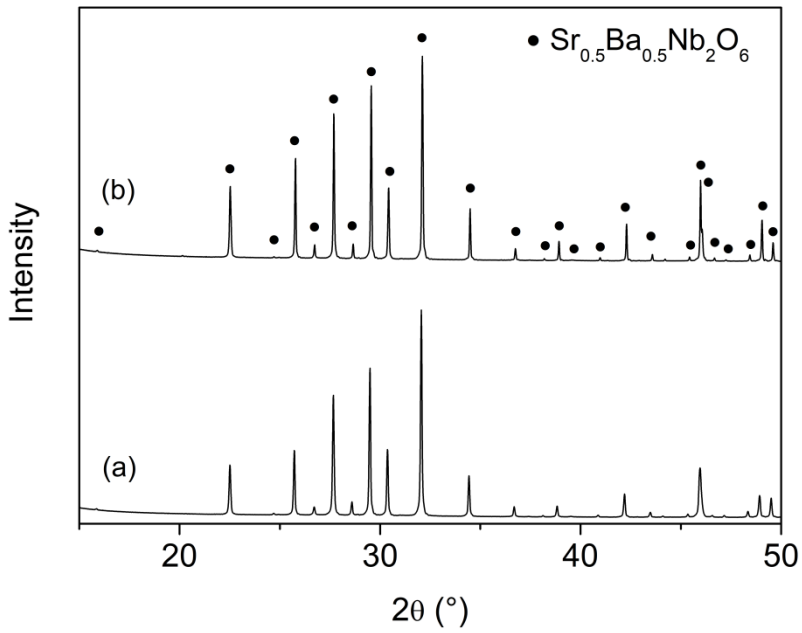

Fig. S4: Room-temperature XRD patterns of SBN+LN-*x* ceramics after sintering at 1300 °C for 1 h (heating-/cooling rate 5 K min^{-1}): (a) $x = 0.1$ (b) $x = 0.2$. The patterns were recorded with a prolonged counting time of 10 s per data point.

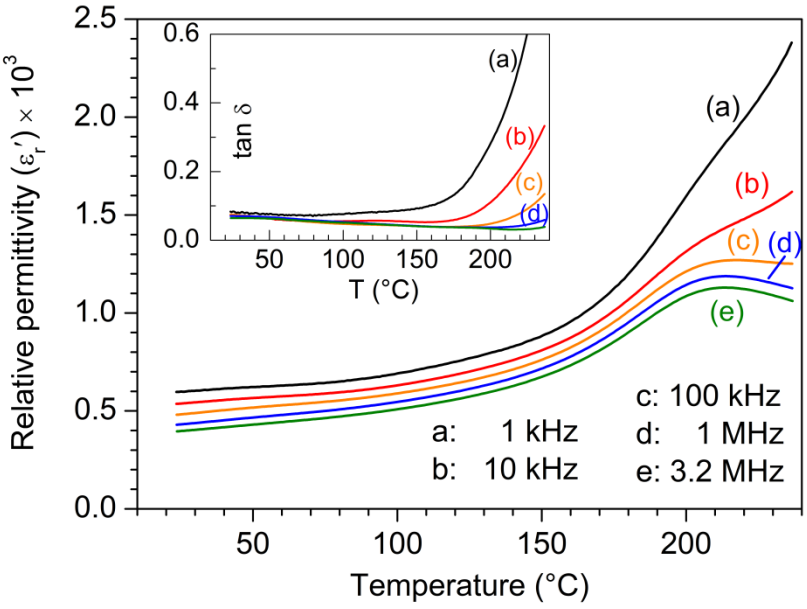

Fig. S5: Temperature dependence of ε_r' and tan δ (inset) at various frequencies for a SBN+LN-0.2 ceramic body sintered at 1100 °C for 1 h.

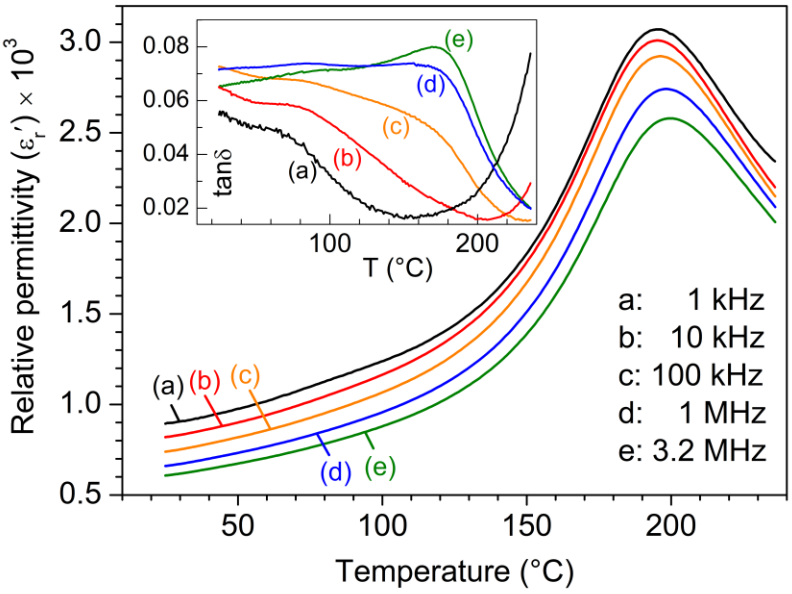

Fig. S6: Temperature dependence of ε_r' and tan δ (inset) at various frequencies for a SBN+LiN-0.2 ceramic body sintered at 1150 °C for 1 h.

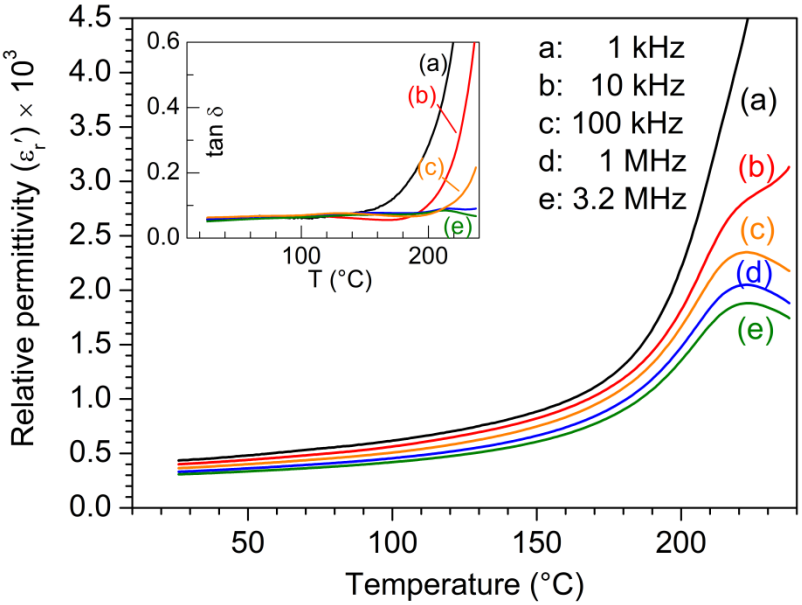

Fig. S7: Temperature dependence of ε_r' and tan δ (inset) at various frequencies for a SBN+LiN-0.2 ceramic body sintered at 1200 °C for 1 h.

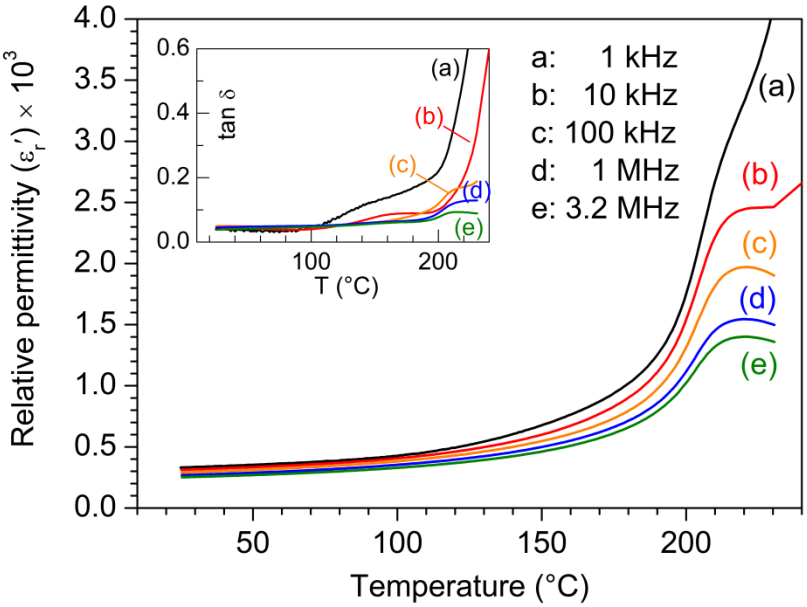

Fig. S8: Temperature dependence of ε_r' and tan δ (inset) at various frequencies for a SBN+LiN-0.2 ceramic body sintered at 1300 °C for 1 h.

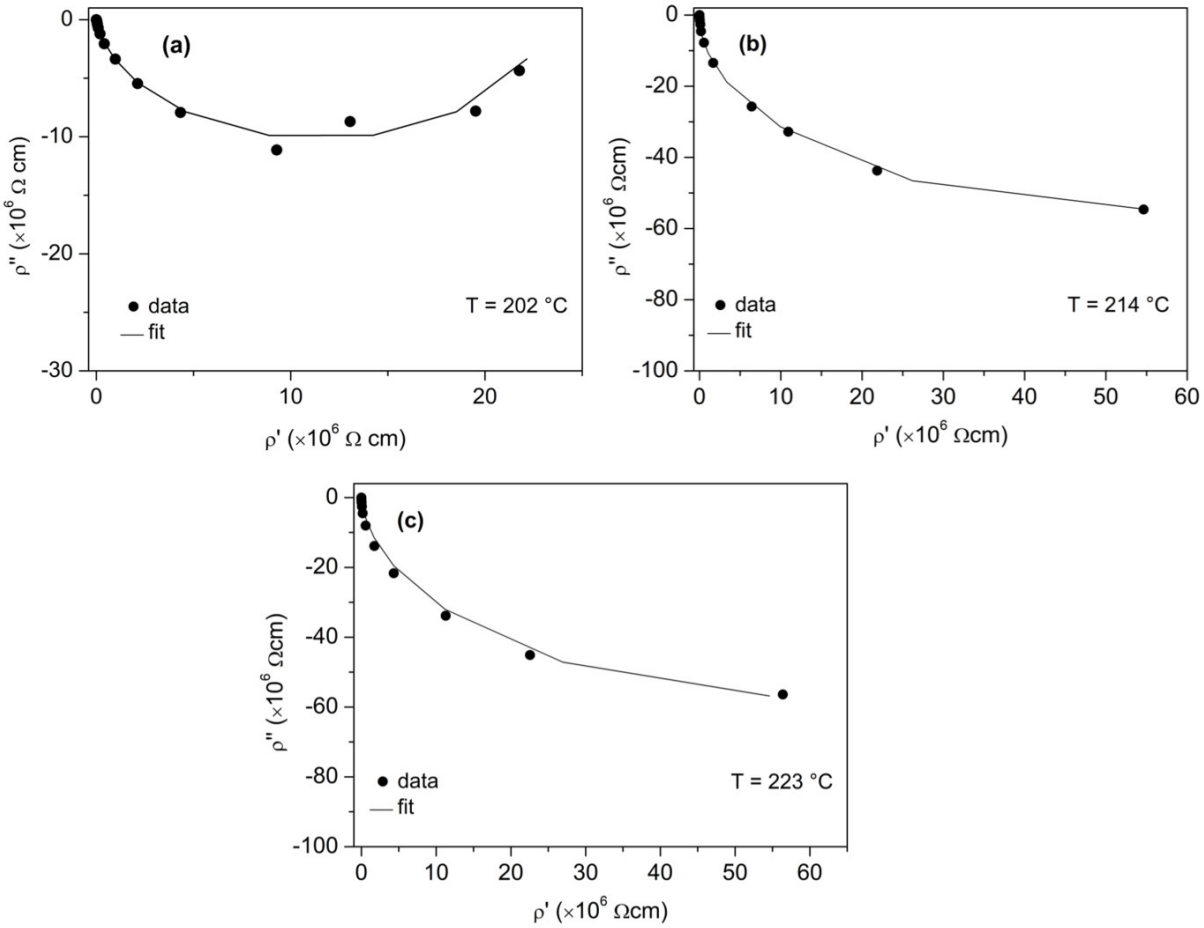

Fig. S9: Cole-Cole plots measured at the indicated temperatures of SBN+LiN-0.1 ceramics sintered for 1 h at different temperatures: (a) 1150 °C (b) 1200 °C, and (c) 1300 °C. Fits were carried out using one parallel connected RC-elements.

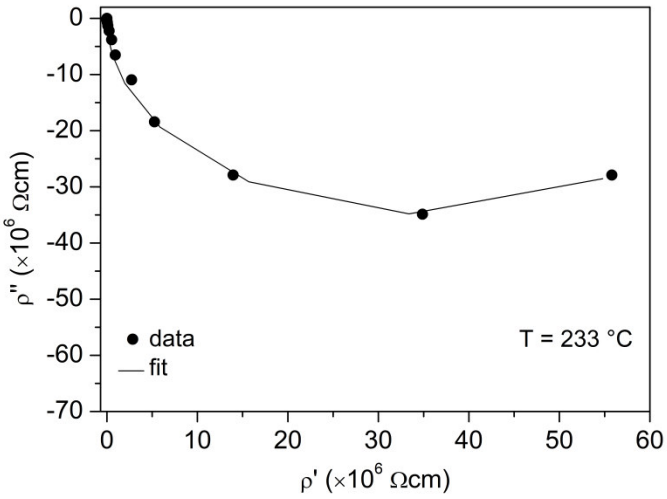

Fig. S10: Cole-Cole plot measured at the indicated temperature of SBN+LiN-0.2 ceramic sintered at 1150 °C for 1 h. The fit was carried out using one RC-elements.